Progress In Electromagnetics Research B, Vol. 100, 1–18, 2023

A Metallic 3D Printed Dual Frequency Dual Circularly Polarized Cross-Slot Waveguide Array Antenna with Improved Grating Lobe

Xianyu Guo and Bing Zhang*

Abstract—A dual frequency dual circularly polarized cross-slot waveguide array working at 4.9 GHz and 5.8 GHz is proposed for wireless communication/airborne weather radar applications. Different from the traditional cross-slotted waveguide antenna, to improve space utilization, two sets of cross-slots are slit on both sides of the longitudinal axis of the waveguide's E-plane to realize dual-frequency operation. When the antenna operates in the TE_{10} mode, the cross-slots on each side radiate left-handed and right-handed circularly polarized electromagnetic waves at two different frequencies, respectively. To suppress grating lobes, phase perturbation structures are periodically loaded in the waveguide to tune the propagation phase constant, thereby changing the effective electric spacing between radiating elements while keeping the antenna a compact physical aperture. The proposed grating lobe suppression method avoids the dielectric loss caused by dielectric loading, eliminates the need for complex array arrangement, and achieves the grating lobe suppression at dual frequencies simultaneously. The metallic 3D printing technology, selective laser melting (SLM), is used to fabricate the antenna in one piece in one run using aluminum alloy. The proposed antenna has gains of 10 dBic and 14.5 dBic with 47% and 69% aperture efficiencies at 4.9 GHz and 5.8 GHz, respectively. It is a capable candidate for air-to-ground (ATG) communication applications.

1. INTRODUCTION

With the improvement of anti-jamming radar and the development of pulsed Doppler radar, rectangular waveguide slot array antennas have been widely used in microwave communication and radar systems [1–9]. It is the preferred antenna choice in airborne radar and satellite communication due to its small size, light weight, high aperture efficiency, and wide-angle beam scanning [10–20] as shown in Fig. 1. A slotted waveguide antenna radiates from the slot on the waveguide surface, which can be slit on either the H-plane or E-plane of the waveguide [21]. By controlling the length of the slot, the radiation of different frequencies can be realized. Such waveguide structure offers significant advantages in terms of weight, volume, and radiation characteristics, which is the reason for its widespread application in radar systems.

Cross-slots waveguide antennas are popular due to their simple structure, light weight, high-power capacity, and circularly polarized radiation [22–31]. By etching a series of cross-slots at the proper position along the longitudinal axis of the waveguide, the circularly polarized radiation of a single frequency is realized [22]. For example, a cross-slotted waveguide array with dual circular polarization at W-band is designed in [23]. The waveguide array contains 16 cross-slots along the E-plane to enable circularly polarized radiation. Such structures achieve dual circular polarization based on the excitation of different input ports. To appropriately deploy the cross-slots at an offset distance from the waveguide's H-plane, the two arms of each cross-slot are bent. However, the array antenna can only work at a single frequency, and nearly half of the waveguide's physical aperture is not radiating,

Received 8 February 2023, Accepted 10 April 2023, Scheduled 15 April 2023
* Corresponding author: Bing Zhang (bzhang0609@hotmail.com).
The authors are with the College of Electronics and Information Engineering, Sichuan University, Chengdu 610065, China.

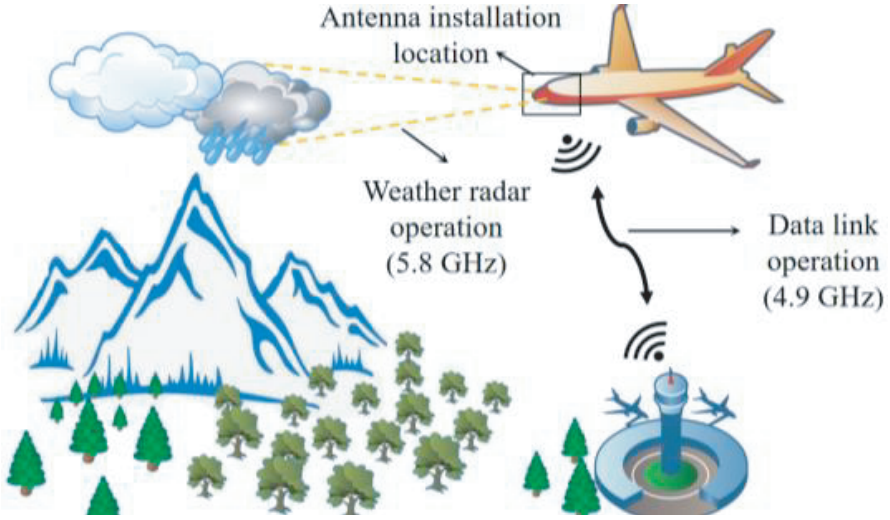

Figure 1. The proposed dual-frequency dual-circularly polarized cross-slotted waveguide array for wireless communications/airborne weather radar system.

resulting in a relatively low aperture efficiency. Moreover, the above-mentioned antenna does not have a flexible phase tuning mechanism, which gives rise to the appearance of grating lobes. An effective way to suppress the grating lobe is to use dielectric loading to shorten the guided wavelength in the waveguide [30]. However, this increases the dielectric loss, reduces the radiation efficiency, and increases the weight and cost of the antenna. To suppress the grating lobe, two arrays are used, one on top of the other with slots staggered to give an effective array element spacing of less than a free-space wavelength in [24] and [29]. Although the antenna's weight is not increased in this way, the two arrays can also only work at the same frequency. The use of metamaterial in slot waveguide arrays to suppress grating lobes is proposed in [32]. By the installation of perturbation elements into the waveguide, the effective wavelength is shortened so that the grating lobe is suppressed. The perturbation element takes the form of an inductive shorting stub and a capacitive post. The stub length and post height are adjusted to provide phase retardation so that the guided wavelength of the array is smaller than the free-space wavelength, thus, grating lobe suppression is achieved. However, the overall volume and weight of the waveguide increase dramatically due to the presence of the shorting stubs, which is not preferred in an airborne system due to the limited payload. Moreover, the planar metamaterial cannot stand the high-power signal in the airborne radar.

In this paper, a dual-frequency dual-circularly polarized cross-slotted waveguide array antenna working at 4.9 GHz and 5.8 GHz is proposed. The 4.9 GHz frequency band can be isolated from the 2.6 GHz frequency to meet the requirements of safety and reliability and is suitable for carrying air-to-ground (ATG) communication business. The radar system of 5.8 GHz has the advantages of all-weather, strong anti-jamming ability, and adaptability to different scenes. As a typical application of the C-band, the 5.8 GHz band can also be used as the weather radar. The proposed dual-band antenna operates at 4.9 GHz and 5.8 GHz, respectively, which can achieve good ATG communication quality while also serving as a weather radar as shown in Fig. 1. By etching different lengths of cross-slots on both sides of the longitudinal axis on the E-plane of the waveguide, we make full use of the waveguide's physical aperture. The proposed antenna realizes the radiation of dual frequency and dual orthogonal circular polarization. Compared with [23], the proposed antenna achieves dual-band radiation on the same aperture, which improves the antenna's aperture efficiency. Compared to other dual-band dual-polarized antennas in [33–35], the proposed antenna has advantages in terms of radiation efficiency, dielectric loss, and application scenarios. The proposed design achieves dual-band dual-circular polarization on the same aperture with high radiation efficiency, while the antenna in [33] achieves linear and circular polarizations on different apertures of the top and bottom surfaces of a SIW structure, respectively, with lower radiation efficiency. Compared with the dual-band dual circularly polarized patch antenna in [34], the proposed antenna takes the form of a slotted waveguide antenna with higher power capacity

and no additional dielectric loss, which is suitable for high power, high gain, and low loss wireless communication systems. In [35], novel dual-band half-mode substrate integrated waveguide (HMSIW) leaky-wave antennas are presented. Comparatively, the proposed antenna has higher power capacity and lower dielectric loss while also achieving dual-band dual-circular polarization, due to the advantage of a slotted waveguide structure. In this design, grating lobes are also effectively suppressed by using the phase perturbation structure, which tunes the effective electric spacing between the array's radiating elements while keeping the array's physical aperture compact. Compared with the design proposed in [32], this antenna uses a phase perturbation structure for the grating lobe suppression of the dual-band dual circularly polarized slot array, which achieves good grating lobe suppression while greatly reducing the array size and obtaining a high aperture efficiency. The equivalent circuit of the phase perturbation structure is modeled. The quantitative relationship between the geometry of the phase perturbation structure and propagation constant is investigated. Moreover, the phase perturbation structure, taking the form of inward protruding iris and outward protruding grooves, also facilitates heat dissipation when the antenna is mounted in the confined space in an aircraft's nose under a high-power scenario. It can ensure the stable operation of the system for a long duty time. The self-cooling characteristic of the antenna is verified by a multiphysics analysis using COMSOL. For the complex geometry of the proposed antenna, the metallic 3D printing technology, selective laser melting (SLM), is used to fabricate the antenna with aluminum alloy. Different from traditional subtractive fabrication technologies, the proposed antenna is printed in one piece in one run, saving the effort of post-processing and assembly, which leads to dramatic cost reduction. In general, the proposed antenna features dual frequency and dual orthogonal circular polarization by the ingenious deployment of the radiating cross-slots; compact size, improved side lobe suppression, and self-cooling by the phase perturbation structure; low cost and light weight by metallic 3D printing technology. It is a capable candidate for the airborne radar system. The quantitatively modeled phase perturbation structure is instructive for engineers to scale the proposed design to different frequencies or to explore the potential of the proposed design for different applications. The paper is organized as follows. Section 2 introduces the design and analysis of the proposed antenna. Section 3 validates the antenna performance by simulation and experiment. Section 4 concludes the paper.

2. DESIGN AND ANALYSIS OF THE PROPOSED ANTENNA

2.1. Design of the Proposed Antenna

The geometry of the proposed antenna is shown in Fig. 2. It is composed of a dual-frequency cross-slots array on the E-plane of the waveguide and a series of phase perturbation structures. The cross-slot arrays on both sides of the longitude axis radiate orthogonal circularly polarized electromagnetic (EM) waves of two frequencies, respectively. The phase perturbation structure realizes the grating lobes' suppression by changing the waveguide's phase propagation constant. To feed the two slot arrays at desired frequencies of 4.9 GHz and 5.8 GHz, we choose a single standard WR-159 waveguide ($a = 40.4$ mm, $b = 20.2$ mm) with an FDP 58 flange at Port1 and Port2. Followed by a section of taper, the waveguide is broadened to a cross-section of $a_1 = 48.8$ mm and $b_1 = 20.2$ mm, which is designed to compensate for the increase of the cut-off frequency by the phase perturbation structure. A wave-splitting iris is designed at an offset $l_p = 14.5$ mm of Port1 to ensure isolation between the two operational frequencies and to achieve good impedance matching. Two linear arrays of cross-slots are designed along the longitude axis on the E-plane of the waveguide, which are responsible for orthogonal CP radiations at 4.9 GHz and 5.8 GHz, respectively. By adjusting the slot lengths l_1 and l_2, the operational frequency of the antenna can be tuned. By mirroring Port1 and Port2, the polarization of the two linear arrays can be reversed.

In order to achieve in-phase radiation from adjacent array elements, cross-slot spacings d_1 and d_2 are designed to be the corresponding guided wavelength, which is larger than the corresponding free space wavelength. Consequently, grating lobes appear. To solve this problem, Eq. (1) should be satisfied:

$$d < \frac{\lambda}{|1 + \sin\theta|}, \tag{1}$$

where d is the slot spacing, λ the free space wavelength, and θ the direction of the main beam. To suppress grating lobes while keeping the radiating aperture compact, phase perturbation structures are

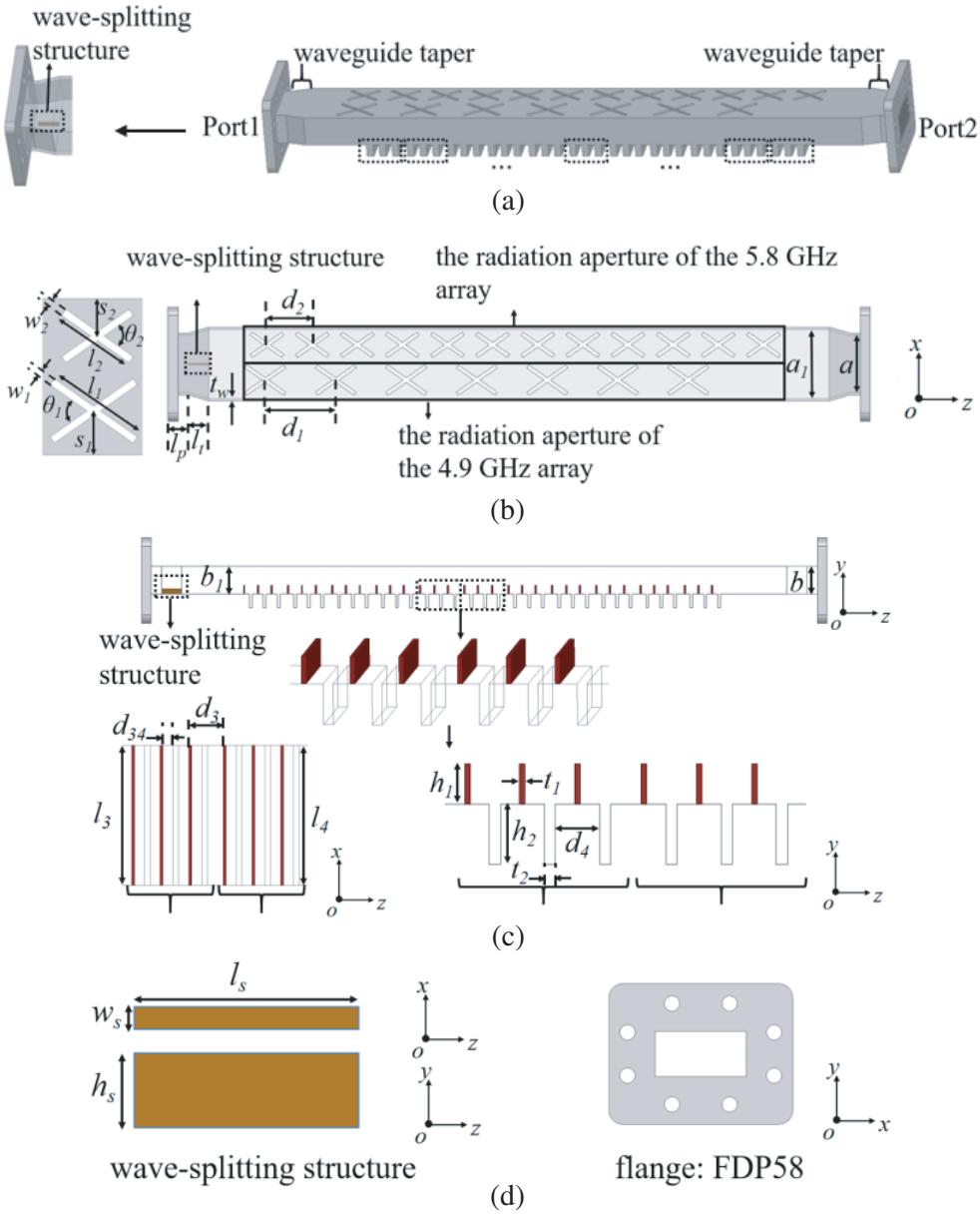

Figure 2. Geometry of the proposed antenna: (a) 3D view, (b) top view, (c) side view (d_3 is the distance between the last iris of a phase perturbation set which consists of three irises and three grooves to the first iris of next phase perturbation set, which is different from the distance $(t_2 + d_4)$ between irises in a set.), and (d) zoomed view of the wave-splitting structure and the flange.

used to tune the electric spacing between cross-slots. Phase perturbation structure consists of a series of inward protruding iris and outward protruding grooves. The propagation phase constant can be tuned by adjusting the height of the iris h_1 and the depth of the groove h_2. By doing this, the electric spacing between cross-slots is tuned for grating lobes suppression. This helps to suppress side lobes while keeping a compact antenna size. The geometric parameters of the proposed antenna are listed in Table 1.

Table 1. Geometric parameters of the proposed antenna (Unit: mm).

Parameters	a	b	a_1	b_1
Value	40.4	20.2	48.8	20.2
Parameters	d_1	d_2	d_3	d_4
Value	50.0	32.0	12.0	8.0
Parameters	d_{34}	h_1	h_2	h_s
Value	3.5	6.5	9.8	3.6
Parameters	l_1	l_2	l_3	l_4
Value	33.7	27.4	48.8	48.8
Parameters	l_p	l_s	l_t	s_1
Value	14.5	14.5	14.5	13.1
Parameters	s_2	t_1	t_2	t_w
Value	10.8	1.0	2.0	1.6
Parameters	w_1	w_2	w_s	/
Value	2.5	2.5	1.0	/

2.2. Analysis of the Proposed Antenna

2.2.1. Orthogonal Circular Polarizations

The cross-slot, as the radiating element, on the E-plane of the waveguide cuts the longitude current to radiate CP EM waves. The arm length of the slot determines the resonant frequency. The axial ratio (AR) is related to the offset position of the cross-slot. Fig. 3 shows the arm's length's effect on the cross-slot's reflection coefficient. In Fig. 3(a), the cross-slot's resonant frequency increases while l_1 decreases, which is also observed in Fig. 3(b) while l_2 varies. With the variation of l_1 and l_2, additional capacitive or inductive components are introduced, thereby shifting the resonant frequency of the cross-slot. In our design, two different arm lengths are set as l_1 =33.7 mm and l_2 =27.4 mm to realize dual frequency operation at 4.9 GHz and 5.8 GHz. When the two linear arrays of cross-slots are deployed on each side

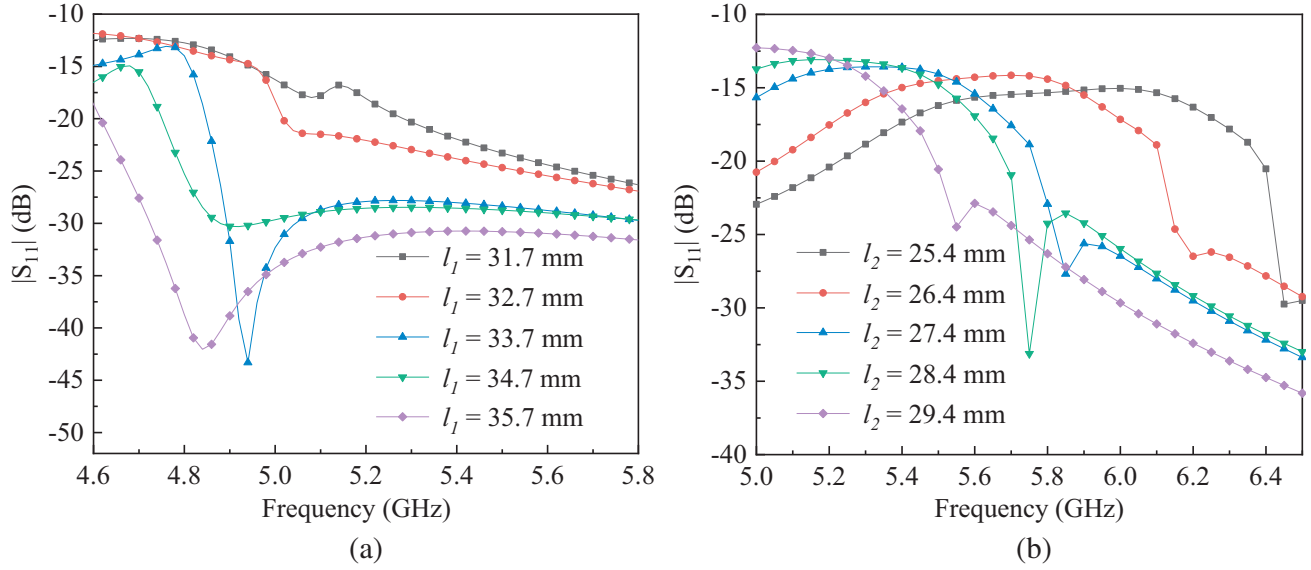

Figure 3. $|S_{11}|$ of the cross-slot when the slot lengths l_1 and l_2 vary: (a) 4.9 GHz and (b) 5.8 GHz.

of the longitude axis of the waveguide's E-plane, adjacent slot arms will overlap with each other and also will extend to the H-plane of the waveguide which gives rise to undesired cross-polarization. To solve this problem, the cross angle is designed as $\theta_1 = \theta_2 = 70°$.

By analyzing the transverse and longitudinal magnetic fields of the TE_{10} mode in the rectangular waveguide, spots could be found where the transverse and longitudinal magnetic fields have equal amplitude and orthogonal phase, which is instructive for the placement of the cross-slot. The offset distance of these spots to the edge of the waveguide's E-plane can be calculated according to [30]

$$s = \frac{a}{\pi} ctn^{-1}\left[\pm\sqrt{\left(\frac{2a}{\lambda}\right)^2 - 1}\right], \tag{2}$$

where a is the width of the waveguide cross-section, and λ is the free space wavelength. When the offset distance varies, the balance of phase and amplitude of the transverse and longitudinal magnetic field is influenced, which is reflected by the variation of the AR. The effect of the offset distance on the AR is shown in Figs. 4(a) and (b), in which the AR varies with s_1 and s_2. However, a large offset distance may lead to the overlap of adjacent cross-slots' arms. Hence, we chose $s_1 = 13.1\,\text{mm}$ and $s_2 = 10.8\,\text{mm}$ for our design.

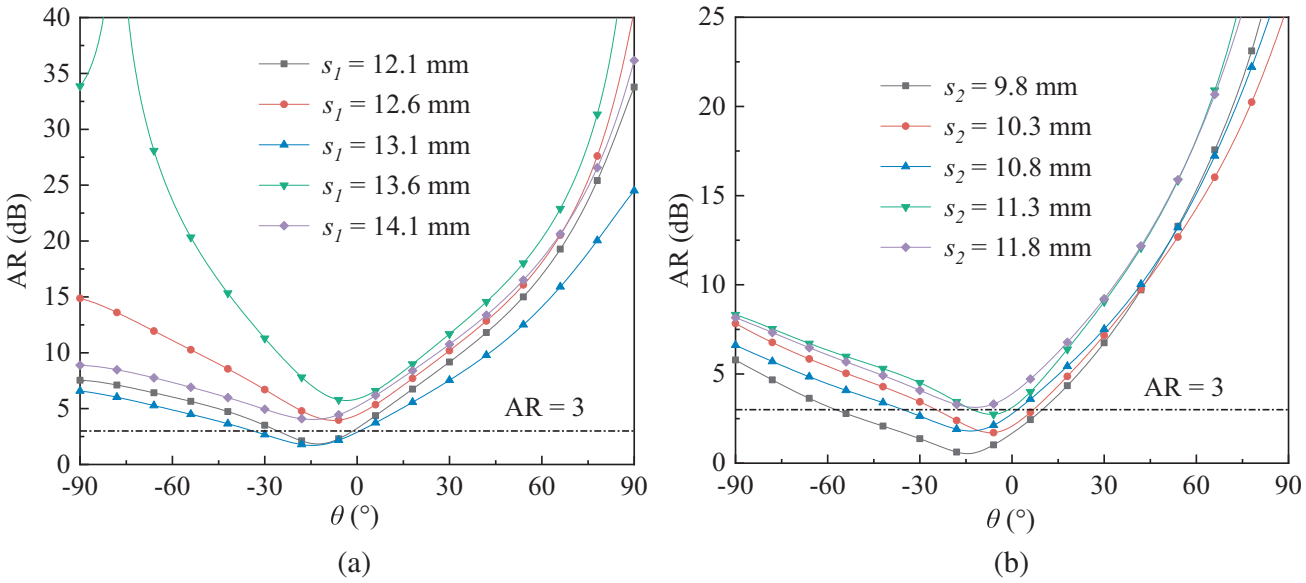

Figure 4. AR of the cross-slot when the offset distance s_1 and s_2 vary: (a) 4.9 GHz and (b) 5.8 GHz ($\varphi = 90°$).

When the TE_{10} mode is excited in the waveguide, surface currents on each side of the E-plane's longitude axis are reversed, which leads to orthogonal CPs. The instantaneous electric field on the cross-slot's aperture (xz-plane) is shown in Fig. 5. It can be observed that the E-field rotates following the left-hand rule at 4.9 GHz for the cross-slot array with $l_1 = 33.7\,\text{mm}$ in Fig. 5(a), while the high-frequency cross-slots do not effectively radiate CP EM waves. right-hand CP EM waves are generated at 5.8 GHz by cross-slot with $l_2 = 27.4\,\text{mm}$ in Fig. 5(b), while the low-frequency cross-slots do not radiate. Due to orthogonal CPs, good isolation is obtained between the two frequencies.

2.2.2. Grating Lobe Suppression

As for an N-element linear array, the main beam direction $\theta_{\max}$ can be calculated as

$$\theta_{\max} = \sin^{-1}\left[\frac{\lambda}{2\pi d}(-\delta \pm 2m\pi)\right] \quad m = 0, 1\ldots, \tag{3}$$

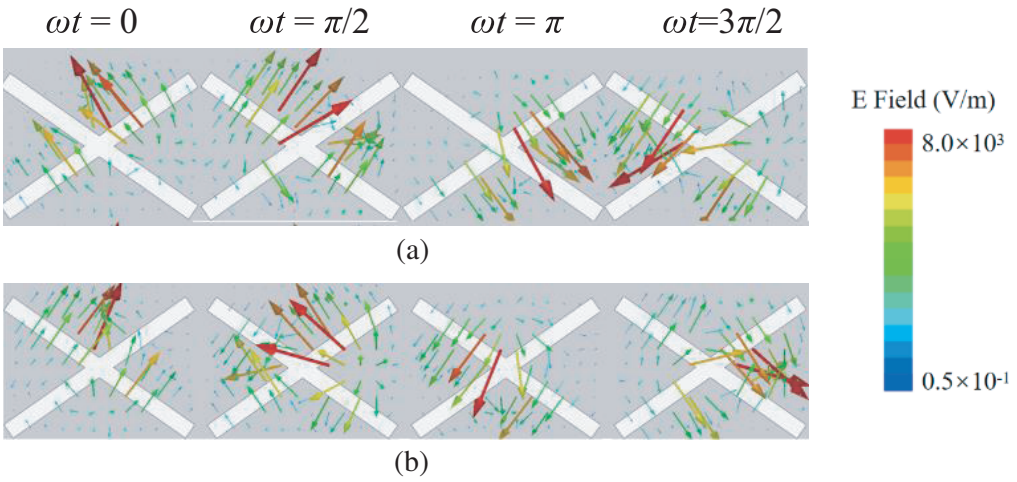

Figure 5. Instantaneous aperture electric field (xz-plane) of the cross-slot (not in-scale): (a) 4.9 GHz and (b) 5.8 GHz.

where d is the element spacing, λ the free space wavelength, δ the phase difference between array elements, and m an integer greater than or equal to 0. Since $\sin^{-1}(x)$ is a multi-value function, there may be more than one angle $\theta_{\max}$ for the same value m. The second and subsequent maximum angles give rise to the phenomenon of grating lobes. It can also be seen from Eq. (3) that as the free space wavelength and phase difference are fixed, the appearance of grating lobes is decided by the array element spacing d. For the cross-slot waveguide array, to make the array elements radiate in phase, the element spacing needs to be set to a guided wavelength at the desired frequency. However, adjusting the array element spacing to one guided wavelength will increase the physical aperture of the antenna and reduce its aperture efficiency. An antenna with an excessively large physical aperture is not suitable for a highly-integrated system. The black dashed line in Fig. 6(a) shows the radiation pattern of a 7-element cross-slot array at 4.9 GHz with the array element spacing of one guided wavelength. It can

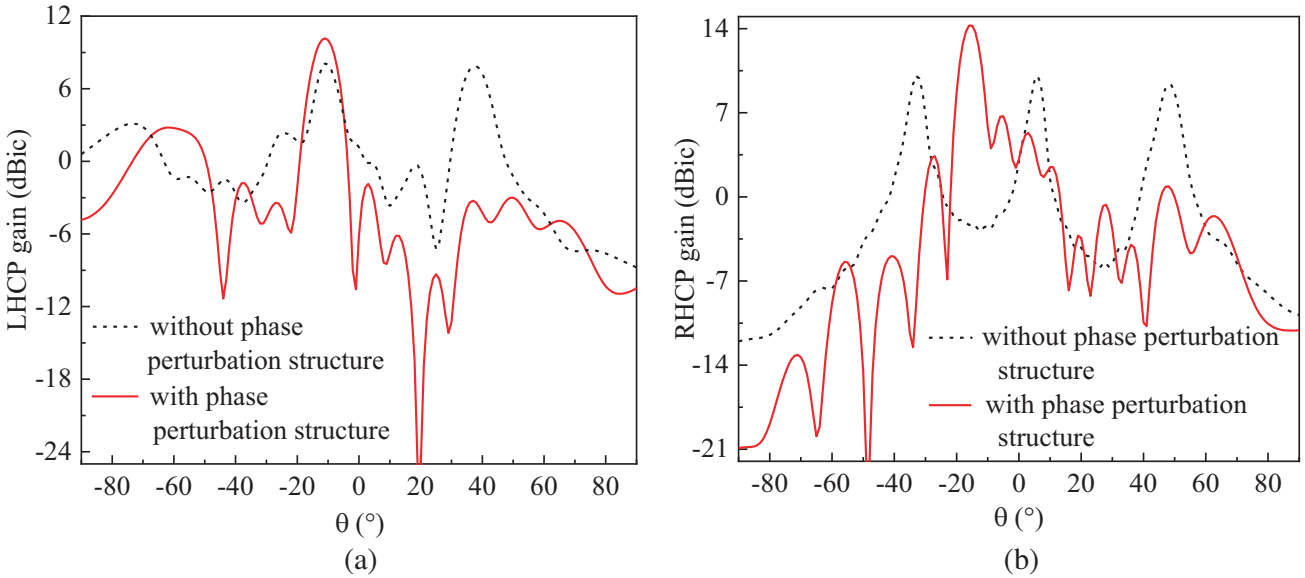

Figure 6. The radiation pattern of the cross-slot linear array with phase perturbation structure and without phase perturbation structure: (a) 4.9 GHz and (b) 5.8 GHz ($\varphi = 90°$).

be seen that the main lobe points to $\theta = -11°$, and a grating lobe points to $\theta = 38°$. The black dashed line in Fig. 6(b) shows the radiation pattern of a 12-element cross-slot array at 5.8 GHz with the array element spacing of one guided wavelength. The main lobe points to $\theta = 6°$, and two grating lobes point to $\theta = -33°$ and $\theta = 42°$, respectively. The grating lobes will cause the dispersion of the radiated power and introduce interference from the undesired targets. To increase the gain in the desired direction and obtain better resolution of the radar system, grating lobes need to be suppressed.

To suppress grating lobes while keeping the antenna a compact structure, the idea is to tune the electric spacing of the array element. Thus, taking the advantage of 3D printing technology in fabricating complex structures, phase perturbation structures, taking the form of inward protruding iris and outward protruding grooves, are designed in the waveguide. In terms of equivalent circuit, the iris is equivalent to a series inductance and two shunt capacitances, and the groove is equivalent to parallel connected inductance and capacitance. The parasitic reactance of the phase perturbation structure leads to the increase of the propagation phase constant of the waveguide's transmission line model, thus the electric spacing between array elements is tuned as shown in Fig. 7. In Fig. 7, Y_0 represents the characteristic admittance of the transmission line; B and B_p are the susceptances of the equivalent capacitive and inductive elements of the rectangular waveguide; $R_s + jX_s$ and $G_s + jB_s$ are the equivalent series impedance and parallel admittance of the radiating slot, respectively; B_a, B_b, B_c, and B_d are the susceptances of the inductance or capacitance of the iris and groove. The equivalent capacitance and inductance values of iris and grooves are mainly determined by the height h_1 of the iris and the depth h_2 of the groove, which means that the magnitude of the resulting phase retardation can be controlled by adjusting h_1 and h_2 to achieve grating lobe suppression. In terms of electric field distribution, the iris and groove elongate the waveguide current, by which an elongated current path is introduced, resulting in a tunable phase delay between array elements as shown in Fig. 8. It can be seen from Fig. 8 that the length of the current path can be changed by adjusting h_1 and h_2.

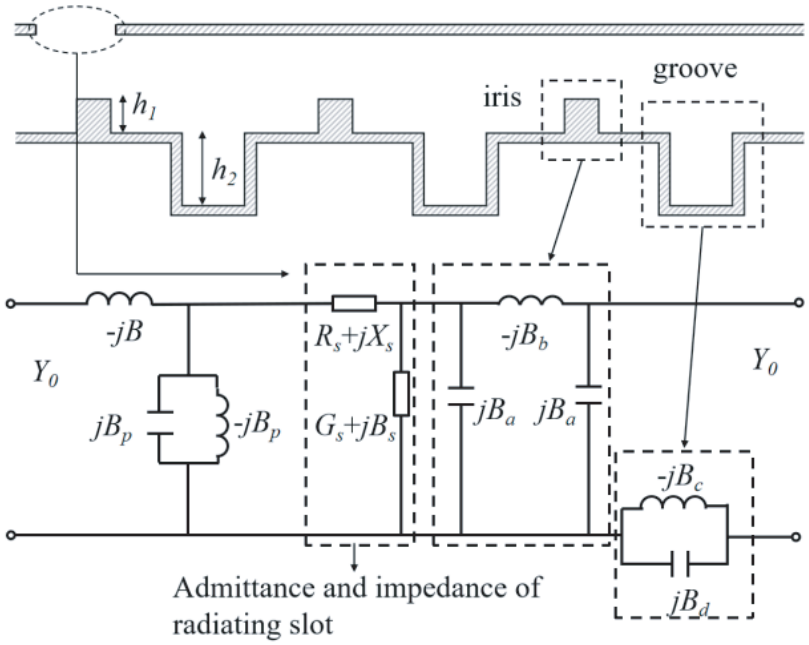

Figure 7. Equivalent circuit of the slotted waveguide array loaded with phase perturbation structure.

The sub-regional method is used to calculate the phase constant of the waveguide loaded with the phase perturbation structure, and the array element spacing d is calculated according to the phase constant of each region. Since the iris and grooves change the width b of the waveguide cross-section, but not the length a, they can be considered as E-plane step discontinuities. A TE_{10}-wave incident in Port1, shown in Fig. 9, excites longitudinal section TE^x_{mn}-wave at all step discontinuities. The superscript x means that the step discontinuity appears in the E-plane (xz-plane). Therefore, we can

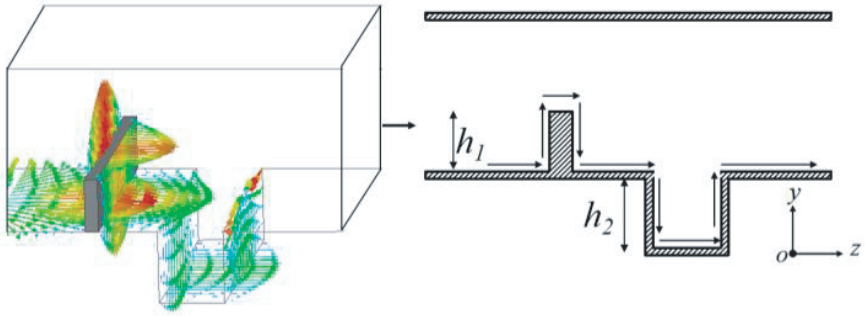

Figure 8. The current distribution of the inner wall of the waveguide loaded with the phase perturbation structure.

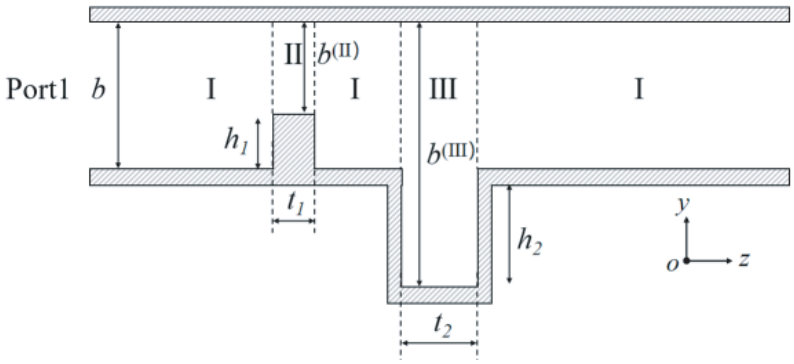

Figure 9. Side view of the waveguide sub-region loaded with a single iris and groove.

calculate the phase constant for each region by judging the TE^x_{mn} modes of each region, which can be achieved by calculating the cut-off frequency of the TE^x_{mn} mode. The cut-off frequency $f_c\,(TE^x_{mn})$ can be calculated as

$$f_c\,(TE^x_{mn}) = \frac{1}{2\pi\sqrt{\mu\varepsilon}}\sqrt{\left(\frac{m\pi}{a}\right)^2 + \left(\frac{n\pi}{b^{(v)}}\right)^2}, \tag{4}$$

where μ is the magnetic permeability, ε the dielectric constant, and $b^{(v)}$ the width of the waveguide cross-section in the region v (v = I, II, and III). For region v that propagates TE^x_{mn} mode, the calculation of the phase constant $\beta_z^{(v)}$ of each region is as follows:

$$\beta_z^{(v)} = \sqrt{k^2 - \left(\left(k_x^{(v)}\right)^2 + \left(k_y^{(v)}\right)^2\right)}, \tag{5}$$

where

$$k = \omega^2\mu\varepsilon, \quad k_x^{(v)} = \frac{m\pi}{a}, \quad k_y^{(v)} = \frac{n\pi}{b^{(v)}}.$$

Therefore, for the slotted waveguide array with three regions of phase perturbation structure loaded between adjacent array elements, the array element spacing d satisfies Eq. (6):

$$\beta_z^{(\mathrm{II})} \cdot 3\,(t_1 + h_1) + \beta_z^{(\mathrm{III})} \cdot 3\left(t_2 + C^{(mn)} \cdot h_2\right) + \beta_z^{(\mathrm{I})} \cdot \left(d - 3(t_1 + t_2) - C_1^{(mn)}\right) = 2\pi, \tag{6}$$

where

$$\beta_z^{(\mathrm{I})} = \frac{2\pi}{\lambda g}$$

λg is the guided wavelength before loading the phase perturbation structure; $C^{(mn)}$ and $C_1^{(mn)}$ are the correction factors when m and n take the modulus value corresponding to the highest order mode in the region III, through which the overall value of the current path in the formula can be adjusted to achieve a more accurate calculation result.

Correction factors $C^{(mn)}$, $C_1^{(mn)}$ in Eq. (6) are adjusted based on the experimental results. Compared with the data in [32], $C^{(10)}$, $C^{(01)}$, $C^{(11)}$, $C_1^{(10)}$, $C_1^{(01)}$, and $C_1^{(11)}$ are taken as 0.8, 1, 1, 4.5, 4, and 18 in our design, respectively. To apply Eq. (6) in our design: (i) The values of f, a, b, h_1, and h_2 need to be determined. The value of a should ensure that the TE_{20} mode does not propagate in the waveguide. For our design, a is adjusted to a_1 48.8 mm, and b is 20.2 mm. For the height h_1 of the iris, when the value is too large, the reflection at Port1 will deteriorates $|S_{11}|$, and the antenna cannot operate normally. Therefore, the value of h_1 is chosen around $1/3b$. For this design, h_1 is 6.5 mm. (ii) The modes judgment of region III is performed according to the above method for different h_2, which is shown in Table 2. According to the modes in region III, the physical spacing between radiating slots d_2 is calculated using Eq. (6). The relationship between d_2 and h_2 is shown in Fig. 10. It can be seen that when $h_2 = 5.66$ mm and $h_2 = 10.3$ mm, d_2 has abrupt changes, which is caused by the excitation of higher-order modes TE_{01}^x and TE_{11}^x in region III. For our design, we choose $d_2 = 30.34$ mm and the corresponding $h_2 = 9.8$ mm to construct the slot array. (iii) After optimization, it is found that the grating lobes at 5.8 GHz are successfully suppressed when $h_2 = 9.8$ mm and $d_2 = 32$ mm as shown in Fig. 6(b). The difference between the calculated d_2 by Eq. (6) and that by simulation is only 1.66 mm. The correctness of Eq. (6) is verified, which gives guidance to engineering designers.

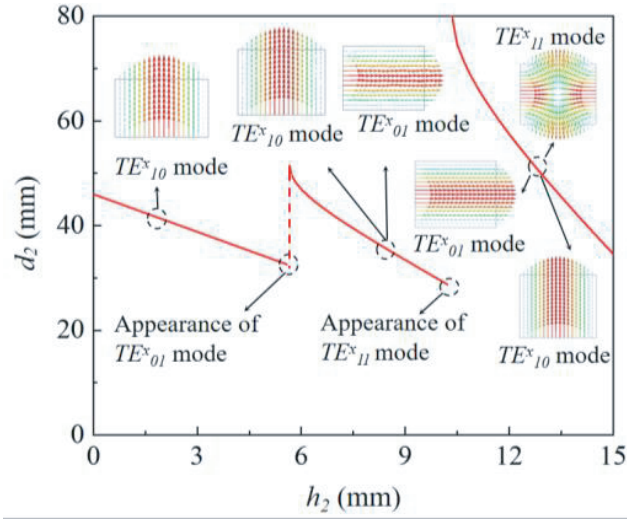

Figure 10. The variation of the array element spacing d_2 with the groove depth h_2 at 5.8 GHz.

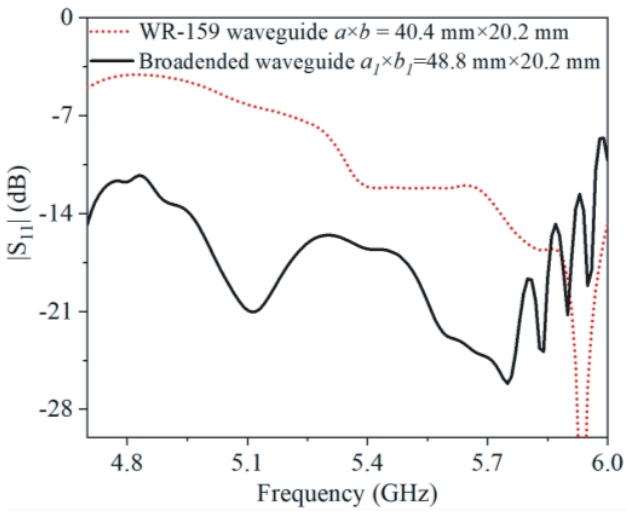

Figure 11. $|S_{11}|$ of the cross-slot array before and after broadening the waveguide.

Table 2. The modes in region III for different depth of the groove at 5.8 GHz.

h_2 (mm)	Modes
0.00–5.66	TE_{10}^x
5.66–10.30	TE_{10}^x, TE_{01}^x
10.30–31.50	TE_{10}^x, TE_{01}^x, TE_{11}^x

In our design, the 4.9 GHz and 5.8 GHz cross-slot arrays share the same physical aperture. Since the 5.8 GHz cross-slot has smaller dimensions than the 4.9 GHz cross-slot, the 5.8 GHz array is firstly designed on one side of the longitude axis of the waveguide, and then the 4.9 GHz array is designed on

the other side of the longitude. For grating lobe suppression at 4.9 GHz, only the element spacing d_1 is adjusted while other geometric parameters are not changed. After optimization, the physical spacing between array elements is set as 50 mm at 4.9 GHz and 32 mm at 5.8 GHz, which satisfies the criteria in Eq. (1). This is also verified by Fig. 6, in which the grating lobe is suppressed when the waveguide is loaded with the iris and groove. In Fig. 6(b), grating lobe suppression is also observed at 5.8 GHz by the phase perturbation structure. As for the design freedom of the main beam angle at 4.9 GHz and 5.8 GHz, the direction of the beam is determined by the array element spacing d according to Eq. (3). The array element spacing d_2 at 5.8 GHz is determined by h_2. When h_2 and d_2 are determined, the main beam direction of the array is also determined at 5.8 GHz. The array element spacing d_1 at 4.9 GHz can be adjusted to determine the main beam direction at 4.9 GHz.

The capacitance of the phase perturbation structure gives rise to the increase of the waveguide's cut-off frequency, resulting in the deterioration of $|S_{11}|$ at 4.9 GHz in Fig. 11. Therefore, the width of the waveguide $a = 40.4$ mm is increased to $a_1 = 48.8$ mm to offset the capacitance from the perturbation and improve impedance matching at 4.9 GHz. It can be seen that the S_{11} is all below -10 dB in the whole frequency band by broadening the waveguide. Simulated radiation patterns and AR at 4.9 GHz are shown in Fig. 12(a). It can be seen that the left hand circular polarization (LHCP) gain of the array at 4.86 GHz, 4.9 GHz, and 4.94 GHz are all 10.0 dBic. The main lobe points to $\theta = -13°$, $\theta = -11°$, and $\theta = -9°$, respectively. The 3 dB AR beamwidth of the three frequencies is 5°. Simulated radiation patterns and AR at 5.8 GHz are shown in Fig. 12(b). The right hand circular polarization (RHCP) gain at 5.76 GHz, 5.8 GHz, and 5.84 GHz are 15.1 dBic, 14.2 dBic, and 13.9 dBic, respectively. As a traveling wave antenna, when the frequency varies within a limited range of around 4.9 GHz and 5.8 GHz, the antenna shows beam scanning capability. The main lobe points to $\theta = -18°$, $\theta = -15°$, and $\theta = -12°$, respectively. The 3 dB AR beamwidth of the three frequencies is 6°.

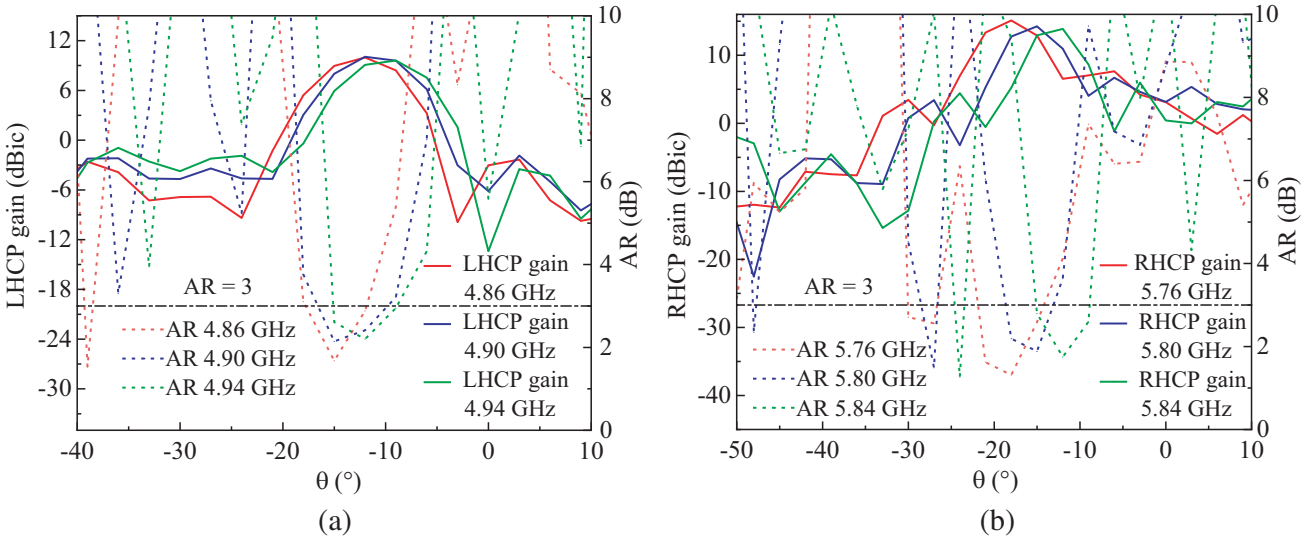

Figure 12. Simulated radiation patterns and AR of the proposed antenna at (a) 4.86 GHz, 4.90 GHz, and 4.94 GHz ($\varphi = 90°$) and (b) 5.76 GHz, 5.80 GHz, and 5.84 GHz ($\varphi = 90°$).

2.2.3. Self-Cooling

The proposed antenna is designed to be used in an airborne radar, which is installed in the confined space of an aircraft's nose. The high-power input signal of the airborne radar can lead to an increased device temperature. The drastic temperature increase can severely affect the stability of the avionics system, whose malfunction may lead to unexpected disastrous air crashes. As a result, the cooling of the device in an avionics system should be seriously considered.

The iris and groove in the proposed antenna can not only work as the phase perturbation structure for grating lobe suppression but also function as the heat radiator because of the increased heat

dissipation area. To evaluate the heat dissipation capability of the phase perturbation structure, a thermal analysis is performed in the commercial software COMSOL. The heat dissipation of the phase perturbation structure is simulated using the heat transfer module in COMSOL. A heat source is mounted on top of the phase perturbation structure, and the dissipated power is 1 W. An ambient temperature of 293 K is set to mimic the environment temperature of the stratosphere. The air inlet velocity is 0.05 m/s, and the outlet pressure is 0 Pa. The simulated body temperatures of the proposed antenna with and without the phase perturbation structure are shown in Fig. 13. It can be seen that the hot spot temperatures in the two cases are 314.2 K in Fig. 13(a) and 341.7 K in Fig. 13(b), respectively. The antenna with the phase perturbation structure can achieve a temperature drop of 27.5 K compared to that without the phase perturbation structure, by which the self-cooling characteristic of the proposed antenna is proved. It can be expected that as the power of the heat source and duty time increases, the effect of the self-cooling characteristic on the device's temperature control would be more obvious. In practical applications, the self-cooling characteristic of the proposed antenna can not only dissipate the heat generated by the EM power in the waveguide but also help to control the temperature of the device which is located in the vicinity of the antenna. The hospitable environment temperature created by the self-cooling characteristic of the proposed antenna can ensure the stable operation of the avionics system during a long duty time, which is vital for aviation safety.

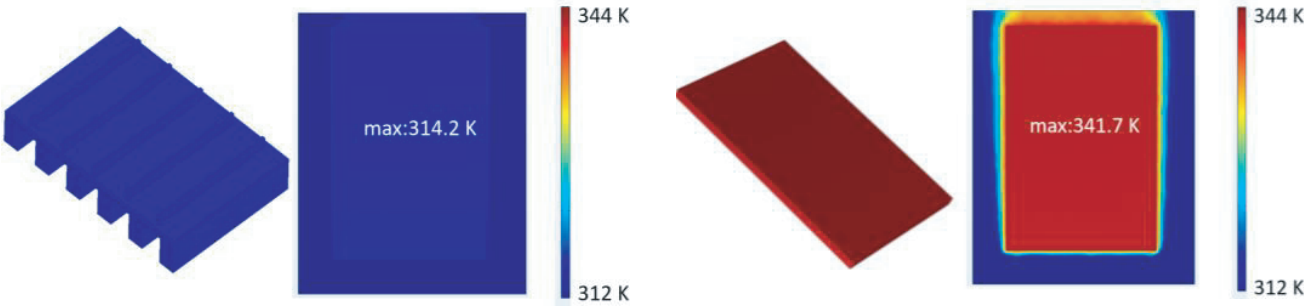

Figure 13. Simulated temperature distribution on a section of the proposed antenna: (a) with the phase perturbation structure and (b) without the phase perturbation structure.

3. FABRICATION AND MEASUREMENT

An antenna prototype is fabricated by SLM using aluminum alloy. Thanks to SLM's capability to fabricate complex structures, the proposed antenna is printed in one piece in one run. Fig. 14 shows photographs of the fabricated antenna. The radiating aperture is shown in Fig. 14(a). The flange surface is milled in Fig. 14(b) for better connection. The wave-splitting iris can be observed. Fig. 14(c) is the side view, in which the outward protruding iris can be seen. The near-field measurement setup is shown in Fig. 15. The antenna is excited from Port1 in measurement, while Port2 is terminated with a matching load.

The simulated and measured $|S_{11}|$ of the proposed antenna are compared in Fig. 16(a). A good consistency is observed. The antenna has an impedance bandwidth of 4.8 GHz–6.0 GHz. The simulated and measured $|S_{21}|$ of the proposed antenna are compared in Fig. 16(b), in which a good consistency can be observed. At 4.9 GHz and 5.8 GHz, a negligible amount of energy is transmitted from Port1 to Port2, indicating that most of the energy is radiated into free space. This is also verified by the antenna's desirable radiation efficiency. The measured and simulated boresight total gains of the proposed antenna are plotted in Fig. 17. The measured and simulated gains agree well in the whole frequency range. The antenna has a total gain of 11.3 dBi at 4.9 GHz and 14.8 dBi at 5.8 GHz. Discrepancies between the simulated and measured antenna gains are from the vibration of the antenna fixture in the near-filed measurement setup. The vibration of the antenna fixture may lead to a tiny tilt of the main beam, hence the difference between simulated and measured antenna gains is observed.

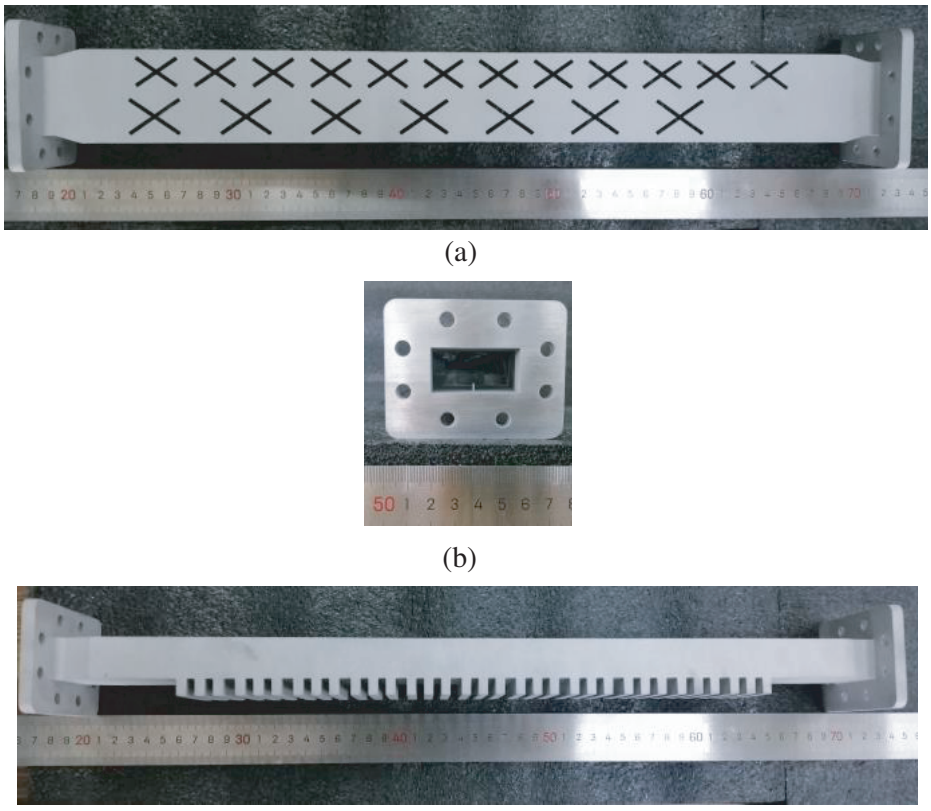

(a)

(b)

(c)

Figure 14. Photographs of the manufactured prototype: (a) top view, (b) flange view at Port1, and (c) side view.

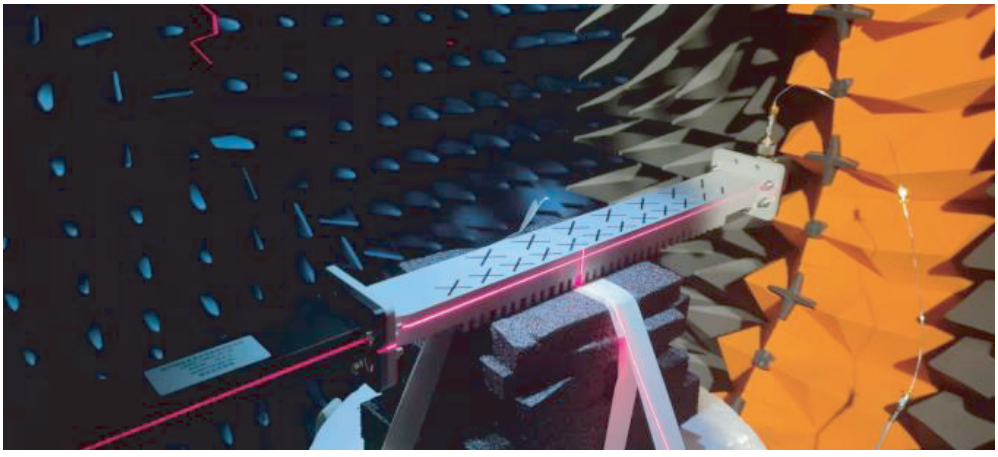

Figure 15. The near-field measurement setup.

As a traveling wave antenna, the proposed antenna has frequency-dependent radiation patterns. Figs. 18(a), (b), and (c) compare the simulated and measured radiation patterns of the proposed antenna at 4.86 GHz, 4.9 GHz, and 4.94 GHz ($\varphi = 90°$). Simulated and measured radiation patterns are in good agreement with the main lobes pointing in the same direction. In measurement, the main lobe at 4.86 GHz appears at $\theta = -13°$, and the LHCP gain is 9.7 dBic. The main lobe at 4.9 GHz appears at

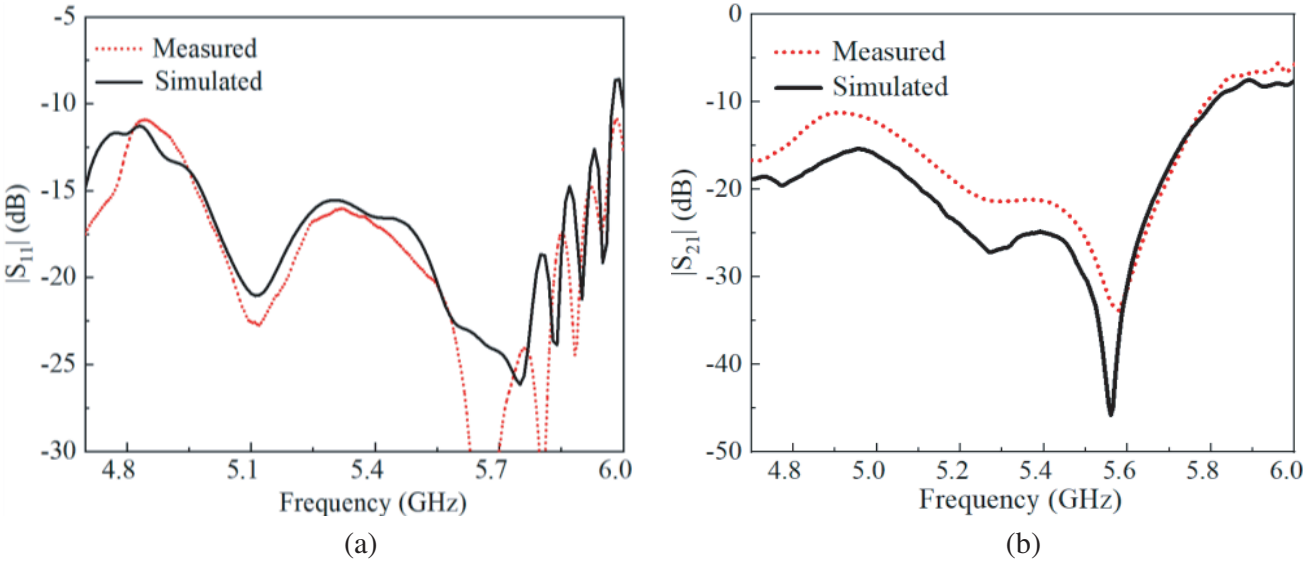

Figure 16. Simulated and measured (a) $|S_{11}|$ and (b) $|S_{21}|$ of the proposed antenna.

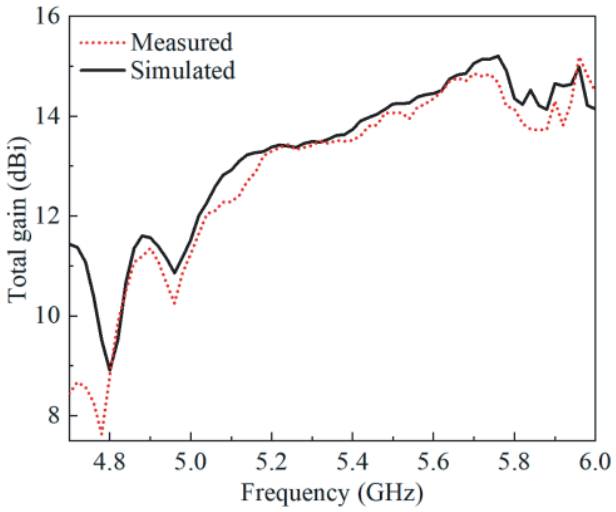

Figure 17. Simulated and measured boresight total gain of the proposed antenna.

$\theta = -11°$, and the LHCP gain is 10.0 dBic. The main lobe at 4.94 GHz points at $\theta = -9°$, and the LHCP gain is 9.1 dBic. Figs. 18(d), (e), and (f) compare the simulated and measured radiation patterns at 5.76 GHz, 5.80 GHz, and 5.84 GHz ($\varphi = 90°$). For measured results, the 5.76 GHz main lobe appears at $\theta = -17°$ with the RHCP gain of 14.5 dBic. The 5.80 GHz main lobe appears at $\theta = -15°$ with the RHCP gain of 14.0 dBic. The 5.84 GHz main lobe appears at $\theta = -12°$ with the RHCP gain of 13.5 dBic. The difference between simulated and measured radiation patterns is due to the fabrication tolerance on the array element spacing d_1 and d_2, which gives rise to the deformation of the synthesized array factor. An annealing process is used to release the structural stress after the antenna is printed, which causes a small deviation of the actual element spacing from the designed one. As a result, the synthesized array factor and radiation patterns are affected. From Fig. 18 it can be observed that the cross-polarization is better than −20 dB in the direction of maximum gain in the frequency ranges of 4.86–4.94 GHz and 5.76–5.84 GHz. The cross-polarization reaches the minimum of −25 dB, which gives the proposed antenna a good anti-jamming capability when being applied in an airborne radar system.

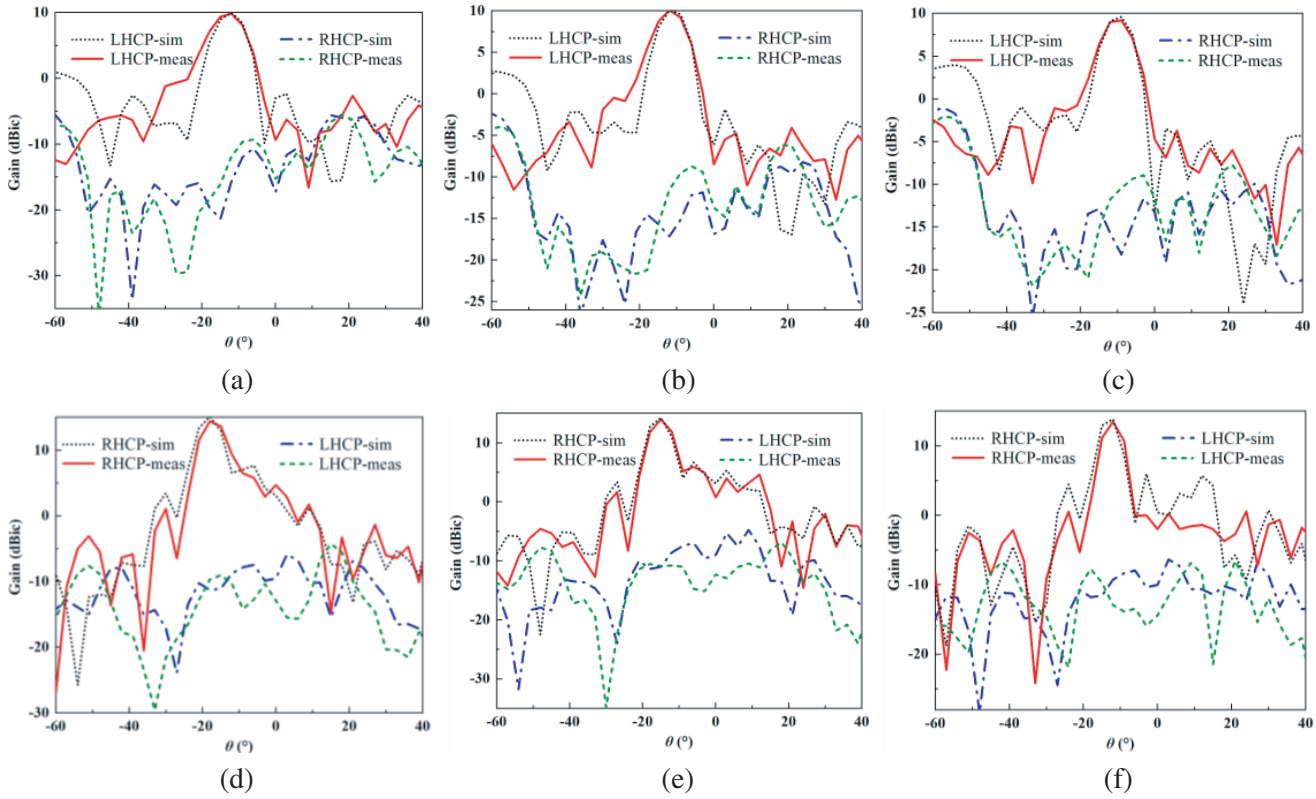

Figure 18. Simulated and measured radiation patterns of the proposed antenna at (a) 4.86 GHz, (b) 4.90 GHz, (c) 4.94 GHz, (d) 5.76 GHz, (e) 5.80 GHz, and (f) 5.84 GHz ($\varphi = 90°$).

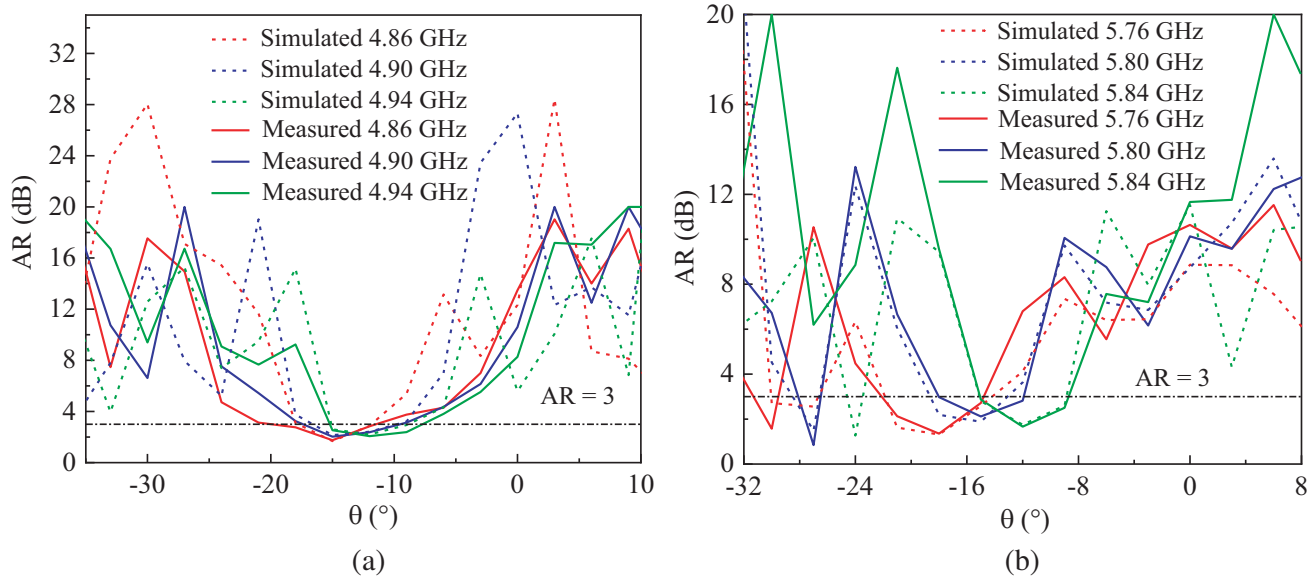

Figure 19. Simulated and measured ARs of the proposed antenna at (a) 4.86 GHz, 4.90 GHz, and 4.94 GHz and (b) 5.76 GHz, 5.80 GHz, and 5.84 GHz ($\varphi = 90°$).

The simulated and measured ARs of the proposed antenna are shown in Fig. 19. It can be seen that the measured AR agrees well with the simulation. In Fig. 19(a), at 4.86 GHz, the simulated 3 dB AR beamwidth is 5°, while it is 7° in measurement. At 4.90 GHz the simulated 3 dB AR beamwidth is 5°, while it is 6° in measurement. At 4.94 GHz, the simulated 3 dB AR beamwidth is 5°, while it is 6° in measurement. In Fig. 19(b), at 5.76 GHz, 5.80 GHz, and 5.84 GHz, the simulated 3 dB AR beamwidths are all 6°, while they are 8°, 6°, and 6° in measurement, respectively. Combining Figs. 18–19, it can be seen that the measured beam scanning range is from −13° to −9° in the first band (4.86–4.94 GHz), and the measured beam scanning range is from −17° to −12° in the second band (5.76–5.86 GHz).

Table 3 compares the proposed antenna with other reported slotted waveguide antennas and dual-band dual-polarized antennas. The proposed antenna features comparable or even better radiation characteristics versus counterparts, especially in terms of aperture efficiency. The proposed antenna has high aperture efficiencies of 47% and 69% in the two operating frequency bands, respectively. It has a compact physical aperture by adopting a phase perturbation structure, which is also effective in grating lobe suppression. Moreover, the phase perturbation structure also has the function of heat dissipating, which helps to save the cost to build a cooling system. The proposed antenna is a capable candidate for the airborne radar application because of its dual frequency dual circular polarization, suppressed grating lobes, high aperture efficiency, and self-cooling function.

Table 3. Comparison between reported works and the proposed antenna.

Ref.	No. of radiating elements	Frequency (GHz)	Peak gain (dBi)	Polarization	Aperture efficiency
[13]	3×2	2.4	6.05	Dual orthogonal LP	11%
[23]	16×8	85	24.0	Dual orthogonal CP	31%
[27]	10×10	25	24.9	Dual orthogonal LP	40%
[29]	26×2	38.6	20.0	Single CP	24%
[33]	88 & 16	9.5 & 15.3	8.0 & 8.0	LP CP	40% & 39%
[35]	10	6.4 & 9.0	11.0 & 10.0	LP	43% & 20%
This work	7 & 12	4.9 & 5.8	11.3 & 14.8	Dual orthogonal CP	47% & 69%

4. CONCLUSION

A dual frequency dual circularly polarized cross-slot waveguide array working at 4.9 GHz and 5.8 GHz is proposed. By deploying two linear arrays on each side of the longitude axis of a waveguide, the waveguide's physical aperture is fully used. The dual-band structure efficiently reduces the volume of wireless communication systems and expands the application scenarios of the antenna. Grating lobes are suppressed by using a phase perturbation structure. The phase perturbation structure tunes the electric spacing between radiating elements, which helps to keep the array compact and obtain high aperture efficiency. This design also confirms the application of a phase perturbation structure in the grating lobe suppression of dual-band dual circularly polarized slot arrays, filling a gap in the grating lobe suppression method for dual-band slot arrays. The quantitative relationship between the phase perturbation structure's dimensions and propagation constant is established, which is instructive for designers. The phase perturbation structure also has the function of heat dissipation, which saves the cost to build the cooling system for the airborne radar. Taking the advantage of 3D printing technology in fabricating complex structures, the proposed antenna is fabricated in one piece in one run, saving the effort of assembling and post-processing, which creates enlarged profit margins for the industry. With these distinctive features, the proposed antenna is expected to serve as a good antenna candidate for airborne radar.

REFERENCES

1. Sakakibara, K., Y. Kimura, J. Hirokawa, M. Ando, and N. Goto, "A two-beam slotted leaky waveguide array for mobile reception of dual-polarization DBS," *IEEE Trans. Vehicle Tech.*, Vol. 48, No. 1, 1–7, Jan. 1999.
2. Wang, W., S. Zhong, Y. Zhang, and X. Liang, "A broadband slotted ridge waveguide antenna array," *IEEE Trans. Antennas Propag.*, Vol. 54, No. 8, 2416–2420, Aug. 2006.
3. Montisci, G., "Design of circularly polarized waveguide slot linear arrays," *IEEE Trans. Antennas Propag.*, Vol. 54, No. 10, 3025–3029, Oct. 2006.
4. Hosseininejad, S. and N. Komjani, "Optimum design of traveling-wave SIW slot array antennas," *IEEE Trans. Antennas Propag.*, Vol. 61, No. 4, 1971–1975, Apr. 2013.
5. Herranz, J., M. Ferrando, A. Valero, and B. Bernardo, "Novel asymmetric T-shaped radiating element for circularly-polarized waveguide slot arrays," *IEEE Trans. Antennas Propag.*, Vol. 69, No. 11, 7452–7461, Nov. 2021.
6. Le, G., "3D printed waveguide slot array antennas," *IEEE Access*, Vol. 4, 1258–1265, 2016.
7. Hirokawa, J., M. Ando, N. Goto, N. Takahashi, T. Ojima, and M. Uematsu, "A single-layer slotted leaky waveguide array antenna for mobile reception of direct broadcast from satellite," *IEEE Trans. Veh. Technol.*, Vol. 44, No. 4, 749–755, Nov. 1995.
8. Armstrong, M. and N. Alexopoulos, "On the design of a circularly polarized waveguide narrow wall linear array," *IEEE Trans. Antennas Propag.*, Vol. 23, No. 2, 244–250, Mar. 1975.
9. Arismar, C., I. F. da Costa, S. Pinna, et al., "A novel dual-polarization and dual-band slotted waveguide antenna array for dual-use radars," *Proc. 10th Eur. Conf. Antennas Propag. (EuCAP)*, 1–4, Davos, Switzerland, 2016.
10. Gatti, R. and R. Rossi, "A dual-polarization slotted waveguide array antenna with polarization-tracking capability and reduced sidelobe level," *IEEE Trans. Antennas Propag.*, Vol. 64, No. 4, 1567–1572, Apr. 2016.
11. Costa, I., S. Cerqueira, and D. Spadoti, "Dual-band slotted waveguide antenna array for adaptive mm-wave 5G networks," *Proc. 11th Eur. Conf. Antennas Propag. (EUCAP)*, 1322–1325, Paris, France, 2017.
12. Rafii, V., J. Nourinia, C. Ghobadi, J. Pourahmadazar, and B. Virdee, "Broadband circularly polarized slot antenna array using sequentially rotated technique for C-band applications," *IEEE Antennas. Wireless Propag. Lett.*, Vol. 12, 128–131, 2013.
13. Li, Y., Z. Zhang, C. Deng, Z. Feng, and M. Iskander, "2-D planar scalable dual-polarized series-fed slot antenna array using single substrate," *IEEE Trans. Antennas Propag.*, Vol. 62, No. 4, 2280–2283, Apr. 2014.
14. Mondal, P. and A. Chakrabarty, "Slotted waveguide antenna with two radiation nulls," *IEEE Trans. Antennas Propag.*, Vol. 56, No. 9, 3045–3049, Sept. 2008.
15. Fang, Z., "The design of S-band low sidelobe rectangular waveguide slot phased array antenna," *Proc. IEEE Asia-Pacific Microw. Conf. (APMC)*, 261–263, Singapore, 2019.
16. Zhang, M., L. Li, and A. Ma, "Analysis of scattering by a large array of waveguide-fed wide-slot millimeter wave antennas using precorrected-FFT algorithm," *IEEE Microw. Wireless Compon. Lett.*, Vol. 15, No. 11, 772–774, Nov. 2005.
17. Ferrando, M., J. Herranz, A. Valero, and V. Rodrigo, "Circularly polarized slotted waveguide array with improved axial ratio performance," *IEEE Trans. Antennas Propag.*, Vol. 64, No. 9, 4144–4148, Sept. 2016.
18. Kim, Y. and H. Eom, "Mode-matching model for a longitudinally slotted waveguide array," *IEEE Antennas Wireless Propag. Lett.*, Vol. 6, 328–331, 2007.
19. Yuan, W., X. Liang, L. Zhang, J. Geng, W. Zhu, and R. Jin, "Rectangular grating waveguide slot array antenna for SATCOM applications," *IEEE Trans. Antennas Propag.*, Vol. 67, No. 6, 3869–3880, Jun. 2019.

20. Lai, Q., W. Hong, Z. Kuai, Y. Zhang, and K. Wu, "Half-mode substrate integrated waveguide transverse slot array antennas," *IEEE Trans. Antennas Propag.*, Vol. 57, No. 4, 1064–1072, Apr. 2009.
21. Stevenson, A., "Theory of slots in rectangular waveguides," *J. Appl. Phys.*, Vol. 19, 24–38, 1948.
22. Hirokawa, J., M. Ando, N. Goto, N. Takahashi, T. Ojima, and M. Uematsu, "A single-layer slotted leaky waveguide array antenna for mobile reception of direct broadcast from satellite," *IEEE Trans. Veh. Technol.*, Vol. 44, No. 4, 749–755, Nov. 1995.
23. Ayoub, F., Y. Tawk, E. Ardelean, J. Costantine, S. Lane, and C. Christodoulou, "Cross-slotted waveguide array with dual circularly polarized radiation at W-band," *IEEE Trans. Antennas Propag.*, Vol. 70, No. 1, 268–277, Jan. 2022.
24. Chatterjee, S., J. Das, and A. Majumder, "Circularly polarized offset center cross slotted array antenna at Ka band," *Proc. IEEE MTT-S Int. Conf. Numer. Electromagn. Multiphys. Model. Optim. (NEMO)*, 1–4, Beijing, China, 2016.
25. Sanchez-Olivares, P., J. Masa-Campos, and E. Garcia-Marin, "Dual-polarization and dual-band conical-beam array antenna based on dual-mode cross-slotted cylindrical waveguide," *IEEE Access*, Vol. 9, 94109–94121, 2021.
26. Sánchez-Olivares, P. and J. Masa-Campos, "Novel four cross slot radiator with tuning vias for circularly polarized SIW linear array," *IEEE Trans. Antennas Propag.*, Vol. 62, No. 4, 2271–2275, Apr. 2014.
27. Yang, Q., et al., "Dual-polarized crossed slot array antenna designed on a single laminate for millimeter-wave applications," *IEEE Trans. Antennas Propag.*, Vol. 68, No. 5, 4120–4125, May 2020.
28. Yin, Y., M. Wang, N. Wu, and W. Wu, "Circularly polarized cross-slot antenna array fed by substrate integrated waveguide," *Proc. 6th Asia-Pacific Conf. Antennas Propag. (APCAP)*, 1–3, Xi'an, China, 2017.
29. Chatterjee, S. and A. Majumder, "Design of circularly polarized waveguide crossed slotted array antenna at Ka band," *Proc. Int. Conf. Microw. Photon. (ICMAP)*, 1–2, Dhanbad, India, 2015.
30. Simmons, A., "Circularly polarized slot radiators," *IRE Trans. Antennas Propag.*, Vol. 5, No. 1, 31–36, Jan. 1957.
31. Sangster, A., "Circularly polarized linear waveguide array," *IEEE Trans. Antennas Propag.*, Vol. 21, No. 5, 704–705, Sept. 1973.
32. Matsui, T., K. Sakakibara, Y. Ikeno, K. Kawaguchi, N. Kikuma, and H. Hirayama, "Control of effective wavelength in the waveguide for grating lobes suppression of slotted waveguide array," *Proc. Int. Workshop Antenna Technol.: Small Antennas and Novel Metamaterials*, 422–425, Chiba, Japan, 2008.
33. Zhang, Q., Q. Zhang, H. Liu, and C. Chan, "Dual-band and dual-polarized leaky-wave antenna based on slotted SIW," *IEEE Antennas Wireless Propag. Lett.*, Vol. 18, No. 3, 507–511, Mar. 2019.
34. Bui, C., N. Nguyen-Trong, and T. Nguyen, "A planar dual-band and dual-sense circularly polarized microstrip patch leaky-wave antenna," *IEEE Antennas Wireless Propag. Lett.*, Vol. 19, No. 12, 2162–2166, Dec. 2020.
35. Rudramuni, K., B. Majumder, P. Rajanna, K. Kandasamy, and Q. Zhang, "Dual-band asymmetric leaky-wave antennas for circular polarization and simultaneous dual beam scanning," *IEEE Trans. Antennas Propag.*, Vol. 69, No. 4, 1843–1852, Apr. 2021.